Two new cubic perovskite oxides Ba3CoSb2O9 and Ba2SrCoSb2O9: Syntheses, crystal structures and magnetic properties

C. Darie, Pierre Bordet, Mélanie Viaud, Catherine Guillot-Deudon, Philippe Deniard, Eric Gautron, Claire Colin, Florence Porcher, Guido Berlanda, Fabrice Bert, et al.

Two new cubic perovskite oxides $Ba_3CoSb_2O_9$ and $Ba_2SrCoSb_2O_9$: syntheses, crystal structures and magnetic properties

Céline Darie[1], Pierre Bordet[1], Mélanie Viaud[2], Catherine Guillot-Deudon[2], Philippe Deniard[2], Eric Gautron[2], Claire Colin[1], Florence Porcher[3], Guido Berlanda[4], Fabrice Bert[4], Philippe Mendels[4], and Christophe Payen[2,*]

[1] *Univ. Grenoble Alpes, CNRS, Grenoble INP, Institut Néel, 38000 Grenoble, France*

[2] *Nantes Université, CNRS, Institut des Matériaux de Nantes Jean Rouxel, IMN, F-44000 Nantes, France*

[3] *Laboratoire Léon Brillouin, CEA Saclay, CNRS UMR12, F-91191 Gif-sur-Yvette, France*

[4] *Laboratoire de Physique des Solides, Université Paris-Saclay, CNRS, 91405 Orsay, France*

* Corresponding author.

E-mail address: christophe.payen@cnrs-imn.fr (C. Payen).

ABSTRACT

Two new cubic perovskite oxides $Ba_3CoSb_2O_9$ and $Ba_2SrCoSb_2O_9$ were prepared and characterized. $Ba_3CoSb_2O_9$ was prepared in polycrystalline form by high-pressure (HP) high-temperature treatment of the hexagonal 6H polytype of $Ba_3CoSb_2O_9$. Polycrystalline samples of $Ba_2SrCoSb_2O_9$ were obtained at ambient pressure by a solid-state reaction method. Combined Rietveld refinements of X-ray and neutron diffraction patterns indicated that HP $Ba_3CoSb_2O_9$ and $Ba_2SrCoSb_2O_9$ both crystallize in a $Fm\bar{3}m$ cubic double perovskite $A_2BB'O_6$ structure with formulae $Ba_2(Sb_{0.83}Co_{0.17})(Co_{0.5}Sb_{0.5})O_6$ and $(Ba_{1.33}Sr_{0.67})Sb(Co_{0.7}Sb_{0.3})O_6$, respectively. Electron diffraction results obtained for $Ba_2SrCoSb_2O_9$ showed no sign of additional periodicity. Weiss temperatures extracted from high-temperature magnetic susceptibility data were $\theta \approx$ -113 K and -118 K for HP $Ba_3CoSb_2O_9$ and $Ba_2SrCoSb_2O_9$, respectively. HP $Ba_3CoSb_2O_9$ displays a weak ZFC-FC magnetic irreversibilty below 8 K. $Ba_2SrCoSb_2O_9$ exhibits a spin freezing at $T_f \approx 6$ K, and μSR and ^{121}Sb NMR data revealed a magnetic transition towards a disordered ground state.

Keywords :
Perovskite oxides
High pressure synthesis
Chemical pressure
Crystal structure
Magnetic properties

1. Introduction

Magnetic frustration in crystallized insulators can result in interesting magnetic states including long-range magnetic orders with quantum fluctuations and quantum paramagnetic states such as quantum spin liquids (QSL) [1]. These exotic magnetic states are studied in transition metal or rare-earth solid state compounds whose crystal structures comprise 2D or 3D spin lattices, e.g., triangular, kagome, honeycomb, pyrochlore, face-centered-cubic (FCC) [2,3]. Even if there exist a great number of frustrated magnetic materials, finding new compounds or new crystal structures that are flexible on their chemical compositions is still of great interest, for instance because it is sometimes difficult to connect theoretical results to experiments on solid state compounds when trying to make a clear diagnosis for a QSL.

In this context, perovskite oxides of the formula $Ba_3M^{2+}Sb^{5+}{}_2O_9$ where M = Ni, Co, Cu have attracted intense research interest in recent years since these materials were identified as candidates for QSL states[4–9]. Their magnetic properties are strongly affected by the crystal chemistry, which itself depends on the synthesis conditions. When polycrystalline or crystal samples are prepared at ambient pressure (AP) conditions, these materials crystallize in a 6H (6-layered hexagonal) perovskite structure. The crystal structures of the AP 6HA polytypes of $Ba_3NiSb_2O_9$ and $Ba_3CoSb_2O_9$ contain non-magnetic Sb_2O_9 pairs of face-sharing octahedra and corner-sharing NiO_6 or CoO_6 octahedra. Magnetic d^8 Ni^{2+} (S=1) or high-spin d^7 Co^{2+} (S=3/2, L=1) ions form triangular lattice layers stacked along the hexagonal *c* axis. 6HA $Ba_3CoSb_2O_9$ is indeed one of the best known experimental realization of equilateral triangular-lattice antiferromagnet with effective spin $S_{eff} = 1/2$ at low temperatures[3]. The unfavorable Sb^{5+}-Sb^{5+} electrostatic repulsion in these 6HA structures is compensated by atom displacement from ideal positions and by a 90° Sb-O-Sb covalent bond[10,11]. The electrostatic repulsive force between $4d^{10}$ Sb^{5+} cations in face-shared octahedra is nonetheless expected to make hexagonal 6HA polytypes relatively unstable. AP $Ba_3CuSb_2O_9$, which contains Jahn-Teller Cu^{2+} ions, has a different 6HB structure, consisting of $CuSbO_9$ dimers of face-sharing octahedra (instead of the Sb_2O_9 bi-octahedra as in the 6HA phase) and corner-sharing SbO_6 octahedra[8]. This compound features a honeycomblike short-range order of Cu^{2+} ions whose spins and orbitals fluctuate down to low-temperatures[12]. Polytypes of $Ba_3NiSb_2O_9$ and of $Ba_3ZnSb_2O_9$ as well can be obtained under high pressure (HP). Upon applying external pressure at high temperatures (HT), $Ba_3NiSb_2O_9$ first transforms from a 6HA phase into a 6HB phase containing $NiSbO_9$ bi-

octahedra and single SbO_6 octahedra[13]. 6HB $Ba_3NiSb_2O_9$ behaves as a spin-1 QSL[4,14]. Upon further increasing pressure, this latter 6HB phase transforms into a cubic polytype, which was also identified as a QSL, containing only corner-sharing NiO_6 and SbO_6 octahedra[4]. No such 6HA-6HB transition is observed for $Ba_3ZnSb_2O_9$, which transforms into a cubic phase at pressures of 3.5 GPa and 4.5 GPa[13]. Chemical pressure is also a useful tool to prepare new structural phases of this family of perovskite oxides. Replacing Ba^{2+} ions with smaller Sr^{2+} ions in AP $Ba_3ZnSb_2O_9$ results in a hexagonal-cubic-tetragonal-monoclinic sequence of structural phases[15]. As for the Co-based perovskites, a study of single-crystals of $Ba_{2.87}Sr_{0.13}NiSb_2O_9$ with the 6HA structure was recently reported[16]. The goal of this latter work was to evaluate the effect of Ba/Sr non-magnetic site disorder on the magnetic properties of the 6HA polytype.

In this work, we explored the effect of both physical and chemical pressures on the structural and magnetic properties of $Ba_3CoSb_2O_9$. Our goal was to prepare new phases that may exhibit quantum magnetic states. Polycrystalline samples of a new cubic perovskite phase of $Ba_3CoSb_2O_9$ were produced by HP-HT treatment of the AP 6HA polytype. In parallel, we investigated the effect of partial substitution of Sr^{2+} for Ba^{2+} in powder samples of AP $Ba_3CoSb_2O_9$. The Sr-substituted $Ba_2SrCoSb_2O_9$ perovskite was obtained using a conventional solid-state reaction method. Room-temperature crystal structures were determined by combined Rietveld refinements of powder X-ray and neutron diffraction patterns. Magnetic properties were investigated through magnetization, μSr and NMR measurements.

2. Materials and methods

2.1 High-Pressure synthesis of $Ba_3CoSb_2O_9$

Polycrystalline samples of $Ba_3CoSb_2O_9$ were prepared by treatment under HP-HT of samples of the AP 6HA phase of $Ba_3CoSb_2O_9$. Powder samples of 6HA $Ba_3CoSb_2O_9$ were first synthetized by a conventional solid-state reaction as described below. Samples of 6HA $Ba_3CoSb_2O_9$ were then placed into gold capsules and heated in either a belt or a Conac 28 anvil-type apparatus. Several syntheses were performed with the belt anvil system in order to determine the best conditions for the syntheses. Single-phased samples of $Ba_3CoSb_2O_9$ were produced during syntheses at 2.9 GPa and at 993 K. Lowering either the pressure (to 1.7 GPa) or the temperature (to 913 K) led to a mixture of 6HA and cubic phases. It is interesting to mention that in any experimental conditions we could not detect the presence of 6HB phase.

2.2 Synthesis of $Ba_{3-x}Sr_xCoSb_2O_9$

Powder samples of $Ba_{3-x}Sr_xCoSb_2O_9$ with targeted compositions x = 0, 0.1, 0.25, 0.5, 0.75, and 1.0 were prepared by heating stoichiometric, pelletized mixtures of high-purity barium carbonate ($BaCO_3$), strontium carbonate ($SrCO_3$), antimony(V) oxide (Sb_2O_5) and cobalt oxide (Co_3O_4) at 1100-1350 °C for several days in air with several intermediate grindings. Pellets were placed on sacrificial powders of the same composition on alumina plates and covered with inverted crucibles to minimize cation volatility at the highest temperature 1350°C. Samples were furnace cooled at the end of the final heat treatment. X-ray diffraction (XRD) indicated that single-phased samples were obtained for nominal x = 0, 0.1, and 1.0, whereas mixtures of crystallized phases (6HA plus cubic) were observed for other nominal compositions. Initial analyses of XRD patterns showed that x = 0 and 0.1 samples crystallized in the hexagonal $P6_3/mmc$ (No. 194) crystal symmetry expected for the 6HA ambient pressure phase of $Ba_3CoSb_2O_9$ [17,18]. All of our x = 1.0 samples crystallized in the cubic $Fm\bar{3}m$ (No. 225) crystal symmetry. Scanning Electron Microscopy (SEM) and Energy X-Ray Dispersive Spectroscopy (EDS) analyses were performed at different positions on the sample surfaces using polished sections. For the homogeneous x = 0 and 1.0 samples atomic ratios of cations were found to be consistent with the nominal ones within the experimental accuracy. Volumetric mass density (ρ) measurements performed at room temperature yielded ρ = 6.650(5) and 6.696(4) g/cm^3 for the phase-pure samples with x = 0 and 1.0, respectively. These values are equal to the densities calculated using the cell parameters derived from X-ray diffraction patterns and the nominal compositions (6.64(8) and 6.7(1) g/cm^3 for x = 0 and 1.0, respectively).

2.3 Structural characterizations

X-ray powder diffraction (XRD) pattern was recorded at room temperature on a Bruker D8 instrument in Bragg-Brentano geometry, equipped with a focusing primary Ge(111) monochromator selecting Cu K-Ł$_3$ radiation (λ = 1.540598 Å). For this wavelength, Co X-ray absorption occurs so that effects of surface roughness on the X-ray intensities were corrected according to the procedure described by P. Suortti[19]. For HP $Ba_3CoSb_2O_9$, neutron powder diffraction (NPD) data were collected at room temperature on the two-axis diffractometer D1B ($\lambda \approx 1.28$ Å) at Institut Laue Langevin (ILL). For $Ba_2SrCoSb_2O_9$, NPD data were collected at 300 K using the 3T2 instrument ($\lambda \approx 1.225$ Å) at Laboratoire Léon Brillouin (LLB, CEA Saclay-CNRS). Le Bail and Rietveld analyses of the XRD and NPD data were performed using

JANA 2006[20] or the Fullprof Suite programs[21]. Because scattering lengths are dependent on the diffraction technique (X-ray or neutron), combined Rietveld refinements of XRD and NPD patterns were performed to provide more meaningful descriptions of the average crystal structures. Neutrons scattering lengths *b* are 5.07, 7.02, 2.49, 5.57, and 5.805 fm for Ba(Z=56), Sr(Z=38), Co(Z=27), Sb(Z=51) and O(Z=8) atoms, respectively. Note that Sr has the highest neutron scattering length and that the Ba-Sr contrasts obtained with X-rays and neutrons are almost opposite; Z(Ba)/Z(Sr) ≈ 1.5 and $b_{Sr}/b_{Ba} \approx 1.4$. Cell metrics were determined from XRD patterns because neutron wavelengths are known with less accuracy than that of X-ray (neutron wavelengths were refined during the joint refinement procedure). The large sample of $Ba_2SrCoSb_2O_9$ used to collect NPD data was also characterized by Selected Area Electron Diffraction (SAED) performed inside a Hitachi H-9000 NAR transmission electron microscope (TEM) operating at 300 kV. Single crystals were selected and oriented along low indexes zone axes. Experimental electron diffraction patterns were compared to those simulated with the JEMS software (https://www.jems-swiss.ch/) considering the crystallographic structure obtained by combined Rietveld refinement of XRD and NPD patterns.

2.4 Magnetic characterizations

Commercial SQUID magnetometers (Quantum Design, MPMS) were used to collect variable-temperature dc magnetization data. The susceptibility was defined as the ratio of the magnetization M to the applied field H, χ = M/H. Muon spin relaxation (μSR) measurements were performed on the GPS instrument used in Veto mode at the Paul Scherrer Institut in zero field (ZF), 50 G weak transverse field (wTF) and 50 G weak longitudinal applied field (LF) geometries, down to 1.55 K for $Ba_2SrCoSb_2O_9$. ^{121}Sb NMR experiments were performed using a standard spin-echo technique on the same sample, in the 1.2 – 60 K temperature range by sweeping the magnetic field in the H = 5-7.2 Tesla range at a 66.238 MHz fixed frequency and at 1.2 K by sweeping the magnetic field in the H = 3.8-5.8 Tesla range at a 49.238 MHz fixed frequency.

3. Results

3.1. Room temperature crystal structures

For both compounds, although all the more intense reflections of the XPD and NPD patterns could be indexed with a cubic perovskite cell of parameter $a_p \approx 4.1$ Å, the presence of

additional weak reflections required the doubling of the cell parameter and a ($2a_p$ x $2a_p$ x $2a_p$) unit cell. All the additional reflections could be indexed with all-odd indices, indicating that the cubic space group is F-centered. Therefore, our starting point for the structure refinements was the $Fm\bar{3}m$ (No. 225) crystal structure (a = 8.1552(2) Å) of the HP phase of $Ba_3NiSb_2O_9$[4]. This structure was described as a $Ba_2BB'O_6$ double perovskite where B (Wyckoff *4a*) and B' (Wyckoff 4b) sites are occupied by Sb and (2/3Ni + 1/3Sb) atoms, respectively (Fig. 1). Ni and Sb atoms were randomly distributed at the B' site. Using this starting model, we obtained a satisfactory combined refinement of XRD and NPD data for HP $Ba_3CoSb_2O_9$ and for $Ba_2SrCoSb_2O_9$. Figures 2 and 3 show the final Rietveld plots. Refined structural parameters and final reliability factors are given in Tables 1 and 2. Cation-anion distances and bond valence sums[22] for both compounds are compared in Table 3. Atomic coordinates and isotropic ADP were kept identical for Ba and Sr atoms at Wyckoff *8c* site, and for Co and Sb atoms at Wyckoff *4a* and *4b* sites. Crystallographic sites were all assumed to be fully occupied. For HP $Ba_3CoSb_2O_9$, Sb/Co site occupancies had to be refined for both *4a* and *4b* sites, and the Sb/Co stoichiometric ratio was constrained to the nominal value of 2.0 (Note that releasing this constraint did not yield significant modifications to the refinement results, so we prefer to keep it). Finally, we found that ≈ 17% of the *4a* site is occupied by Co^{2+} cations, while Co^{2+} and Sb^{5+} cations share the *4b* site in almost equal proportions. For the Sr-substituted compound, the best refinement was obtained when the Wyckoff *4a* site is occupied only by Sb atoms. We refined the occupancies of the Ba/Sr (*8c*) and Co/Sb (*4b*) sites, which yielded cation stoichiometric ratios close to the nominal ones. In these double perovskite descriptions, the chemical formulae are $Ba_2Co_{2/3}Sb_{4/3}O_6$ and $Ba_{4/3}Sr_{2/3}Co_{2/3}Sb_{4/3}O_6$ for the HP and Sr-substituted compounds, respectively.

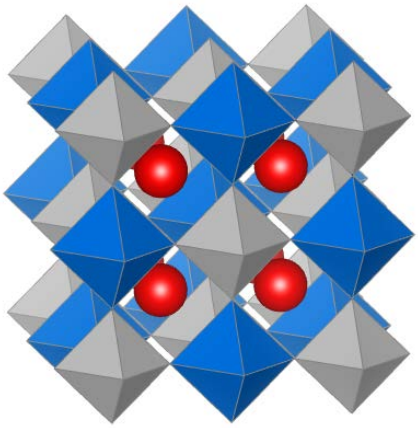

Figure 1. Room temperature $Fm\bar{3}m$ crystal structure adopted by HP $Ba_3NiSb_2O_9$ (a = 8.1552(2) Å)[4]. Blue octahedra are occupied by Sb atoms sitting on Wyckoff *4a* sites. Grey octahedra are randomly occupied by Ni and Sb atoms at Wyckoff *4b* sites. Red spheres represent Ba atoms. This structure has an ordered rock salt arrangement of grey and blue octahedra, giving rise to two interpenetrating FCC sublattices of octahedra.

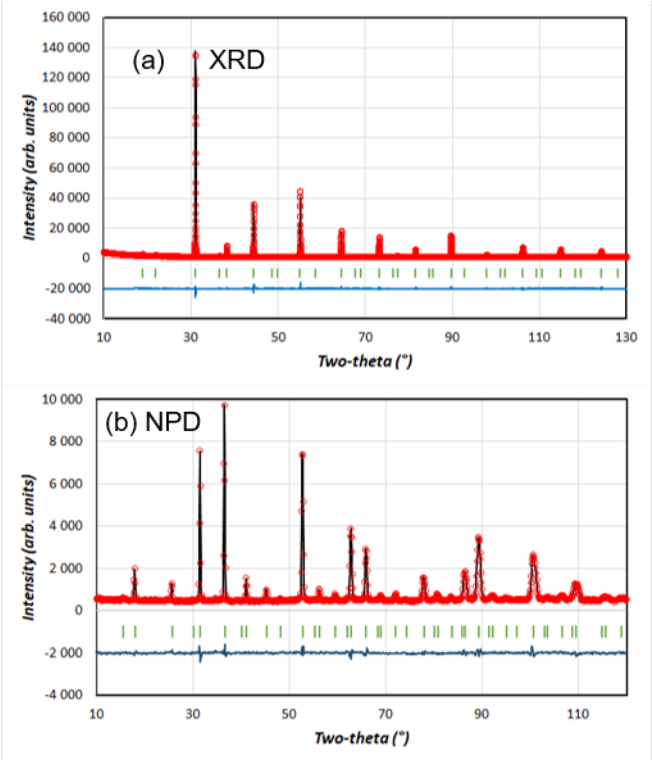

Figure 2. Final combined Rietveld refinement plots of the (a) XRD (λ=1.540598 Å) and (b) NPD (λ = 1.28 Å) data for HP $Ba_3CoSb_2O_9$. Black solid curves are the best fits obtained with space group $Fm\bar{3}m$.

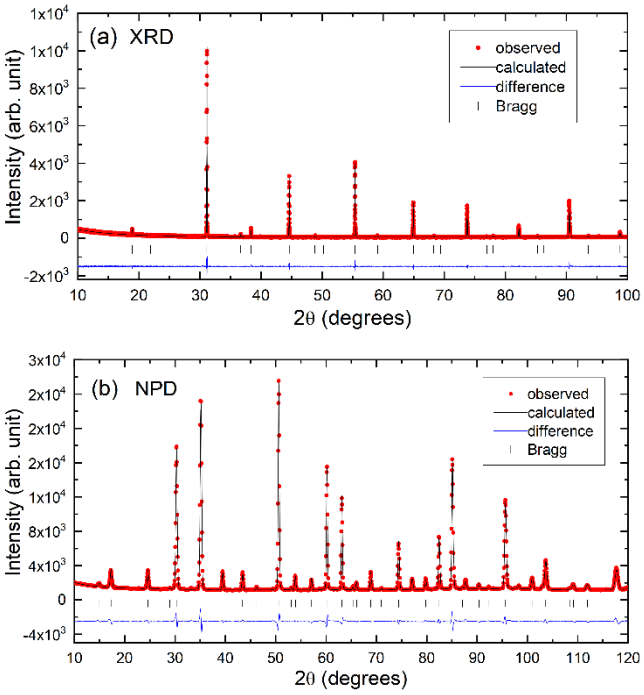

Figure 3. Final combined Rietveld refinement plots of the (a) XRD (λ = 1.540598 Å) and (b) NPD (λ = 1.22901 Å) data for $Ba_2SrCoSb_2O_9$. Black solid curves are the best fits obtained with space group $Fm\bar{3}m$.

Table 1. Refined structural parameters and final agreement factors for HP $Ba_3CoSb_2O_9$ derived from X-ray and neutron diffraction data collected at 300 K. Refinements were performed in a $A_2BB'O_6$ double perovskite model with space group $Fm\bar{3}m$.

Atom	Site	*x*	*y*	*z*	U_{iso} (Å^2)	Occupancy
Ba	8c	1/4	1/4	1/4	0.0144(2)	1
Sb/Co	4a	1/2	1/2	1/2	0.0091(4)	Sb:0.834(5) Co:0.166(-)
Co/Sb	4b	0	0	0	0.0160(5)	Sb:0.502(5) Co:0.498(-)
O	24e	0.2546(5)	0	0	0.0170(3)	1

Space Group : $Fm\bar{3}m$ (No. 225); a = 8.17330(5) Å
Chemical formula: $Ba_2(Sb_{0.83}Co_{0.17})(Co_{0.50}Sb_{0.50})O_6 = Ba_2Co_{0.67}Sb_{1.33}O_6$
XRD: GOF=2.29, Rp= 5.08,wRp = 6.57
NPD: GOF=1.47, Rp = 4.38, wRp = 5.57
Over all: GOF= 2.22, Rp= 5.04,wRp = 6.52

Table 2. Refined structural parameters and final agreement factors for $Ba_2SrCoSb_2O_9$ derived from X-ray and neutron diffraction data collected at 300 K. Refinements were performed in a $A_2BB'O_6$ double perovskite model with space group $Fm\bar{3}m$.

Atom	Site	*x*	*y*	*z*	U_{iso} (Å^2)	Occupancy
Ba/Sr	8c	1/4	1/4	1/4	0.01453(11)	Ba:0.6648(3) Sr: 0.3352(-)
Sb	4a	1/2	1/2	1/2	0.0063(2)	1
Co/Sb	4b	0	0	0	0.0087(4)	Co:0.6982(2) Sb:0.3018(-)
O	24e	0.25388(11)	0	0	0.01792(7)	1

Space Group : $Fm\bar{3}m$ (No. 225); a = 8.11653(2) Å
Chemical formula: $(Ba_{1.33}Sr_{0.67})Sb(Co_{0.70}Sb_{0.30})O_6 = Ba_{1.33}Sr_{0.67}Co_{0.70}Sb_{1.3}O_6$
XRD: GOF = 1.15 Rp = 7.59 wRp = 10.23
NPD: GOF = 3.76 Rp = 3.12 wRp = 4.23
Over all: GOF = 1.83 Rp = 4.35 wRp = 4.97

Table 3. Principal bond lengths for HP $Ba_3CoSb_2O_9$ and $Ba_2SrCoSb_2O_9$ derived from the joint refinement of X-ray and neutron diffraction data with space group $Fm\bar{3}m$ and bond valence sums for the cations[22].

Atoms	site	Distance (Å) for HP $Ba_3CoSb_2O_9$	BVS	Distance (Å) for $Ba_2SrCoSb_2O_9$	BVS
Ba/Sr - O	8c	2.88994(6)	Ba:2.34	2.86980(2)	Ba:2.47/Sr:1.58
Sb/Co - O	4a	2.006(4)	Sb:5.05/Co:2.52	1.9976(9)	Sb:5.14
Sb/Co - O	4b	2.081(4)	Sb:4.12/Co:2.06	2.0606(9)	Sb:4.73/Co:2.21

Cell parameters refine to 8.1733 Å and 8.1165 Å for the HP and Sr-substituted compounds, respectively. In such cubic $A_2BB'O_6$ double perovskites, one has: $a.\sqrt{2} = 4.(r_O + r_A)$, where a is the cell parameter and r_O, r_A are the ionic radii of oxygen anions (taken as 1.4 Å) and A site cations. Thus for the HP phase, one finds a A site radius of 1.49 Å, which is much smaller than the 1.61 Å Shannon radius of Ba^{2+} cations in 12-fold coordination[23]. On

the other hand, for the B sites, one has: $a = 4.r_O + 2.(r_B + r_{B'})$, where r_B and $r_{B'}$ are the radii of the B and B' cation sites, respectively. In this case, one finds $r_B + r_{B'}$=1.29 Å, to be compared to 1.23 Å calculated from Shannon radii. This indicates that most of the compression brought about by the application of pressure to stabilize the HP cubic double perovskite phase is supported by the Ba^{2+} A site cation. Indeed, when comparing with the ambient pressure 6HA phase[17], the average Ba-O distance shrinks from 2.957 Å to 2.890 Å with the application of pressure, while the B-O and B'-O distances hardly change, with their average decreasing only from 2.05 to 2.04 Å (1.997 to 2.006 Å for B, 2.107 to 2.081 Å for B' for the AP 6HA and HP phases, respectively). This reveals clearly that the effect of applied pressure is non uniform on the different cation sites and the deformation due to compression is essentially taken by the A site. Therefore, it can be expected that the same structure can be stabilized by the partial replacement of Ba^{2+} cations by the much smaller Sr^{2+} cations (r = 1.44 Å[23]) on the A site, and this is what we observed. The only refined atomic coordinate, namely the *x* parameter of the O atom at Wyckoff *24e* position (Table 2), is similar for both compounds. These values are slightly higher than the 0.25 one which would be expected for a ABO_3 perovskite structure without cationic order on the B site. Here, the oxygen anions are displaced from this position towards the sites occupied by the smaller B cations. Since the Shannon radii of Co^{2+} and Sb^{5+} are 0.65 Å and 0.6 Å, respectively[23], the oxygen anions move towards the *4a* sites which are mainly or totally occupied by Sb^{5+} cations. Replacing 1/3 of Ba^{2+} cations with Sr^{2+} reduces the average A-O distance to 2.870 Å, i.e. smaller than the Ba-O distance in the HP phase, which yields also a cell parameter substantially smaller for the Sr substituted phase 8.117 Å compared to 8.173 Å. For the B/B' sites, the average B/B'-O distance changes only little from 2.043 to 2.029 Å. These observations indicate that in the present case, the Ba/Sr substitution behaves like an internal chemical pressure, since it allows to stabilize the same structure type through a very similar mechanism.

In order to determine whether or not there are symmetry lowering or supercell reflections corresponding to a Ba/Sr or Co/Sb long range periodic order, SAED patterns were acquired on several crystals along different crystal orientations for the $Ba_2SrCoSb_2O_9$ compound. SAED allowed to characterize individual crystallites. As shown in Fig. 4, it was possible to explain all of our SAED patterns taking account the crystallographic structure obtained by the aforementioned combined Rietveld refinement. No additional spot that could have been due to superstructure or additional periodicity was observed. The results obtained on

single crystals by SAED are fully consistent with the $Fm\bar{3}m$ double perovskite structure described in Table 2.

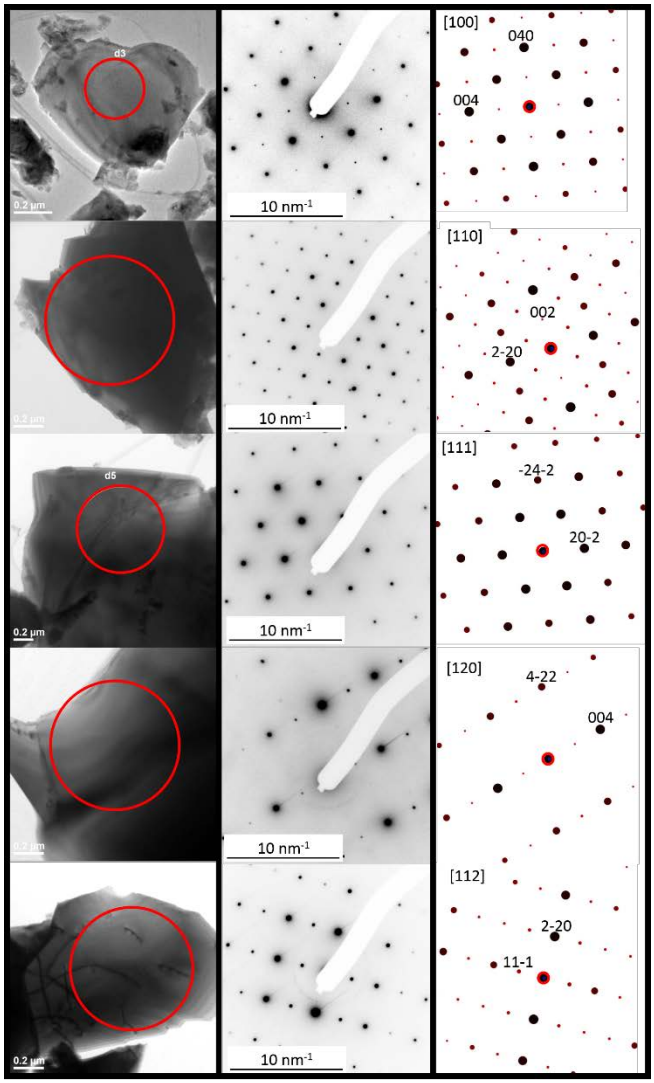

Figure 4. Experimental (center column) and simulated (right column) SAED patterns of a $Ba_2SrCoSb_2O_9$ sample along the zone axes [100], [110], [111], [120], and [112]. Selected area are shown on the TEM images in the left column. Simulated patterns were obtained using the $Fm\bar{3}m$ crystal structure given in Table 2.

3.2. Magnetic susceptibility

Figure 5 shows the inverse magnetic susceptibilities as a function of temperature, $1/\chi(T)$, for HP $Ba_3CoSb_2O_9$ and $Ba_2SrCoSb_2O_9$. The compounds exhibit similar behavior above ≈ 20 K. In the high-temperature range 200-300 K, the data display Curie-Weiss behavior, $\chi = C/(T-\theta)$. Effective magnetic moments are 5.5 and 5.4 μ_B/Co-atom for HP $Ba_3CoSb_2O_9$ and

$Ba_2SrCoSb_2O_9$, respectively. These values are comparable to that observed in 6HA $Ba_3CoSb_2O_9$ with the same temperature fittings range (5.6-5.7 μ_B/Co-atom [17,24]) and in other Co-based perovskites[25]. Experimental magnetic moments are significantly higher than the spin-only value for S = 3/2 (3.87 μ_B) because octahedral high-spin Co^{2+} has an orbitally nondegenerate $^4T_{1g}$ ground state[26]. The fitted Weiss temperatures are -113(1) and -118(1) K for HP $Ba_3CoSb_2O_9$ and $Ba_2SrCoSb_2O_9$, respectively. The negative Weiss temperatures suggest dominant antiferromagnetic interactions between Co^{2+} ions. The positive deviation of $1/\chi$ from the high temperature Curie-Weiss behavior observed below 150 K is also consistent with AF couplings.

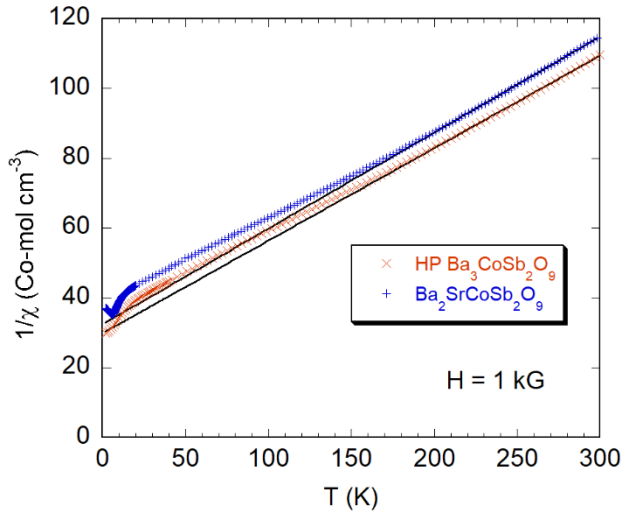

Figure 5. Inverse dc magnetic susceptibility $1/\chi$ versus temperature *T* for HP $Ba_3CoSb_2O_9$ and $Ba_2SrCoSb_2O_9$. Data were acquired under an applied magnetic field of 1 kG. Solid lines denote Curie-Weiss fits from 200 to 300 K.

The low-temperature magnetic susceptibility data measured in a small applied magnetic field of H = 100 G can be seen in Figure 6. For both compounds, the zero-field-cooled (ZFC) and field-cooled (FC) data coincide and increase with decreasing temperature down to 6-8 K indicating paramagnetic behaviour without ferro or ferrimagnetic impurities. For HP $Ba_3CoSb_2O_9$ a small difference between the ZFC and FC measurements is visible below 8 K. There is no peak anomaly in the ZFC susceptibility at 8K or below, in contrast to what is expected for a spin glass transition [27]. For $Ba_2SrCoSb_2O_9$, a ZFC-FC bifurcation occurs below the temperature T_f = 6.1 K at which a maximum is observed in the ZFC trace. This latter feature, which is typical for a spin freezing occurring at T_f = 6.1 K, prompted us to further

investigate the low-temperature magnetic state of $Ba_2SrCoSb_2O_9$ using microscopic probes, as described below.

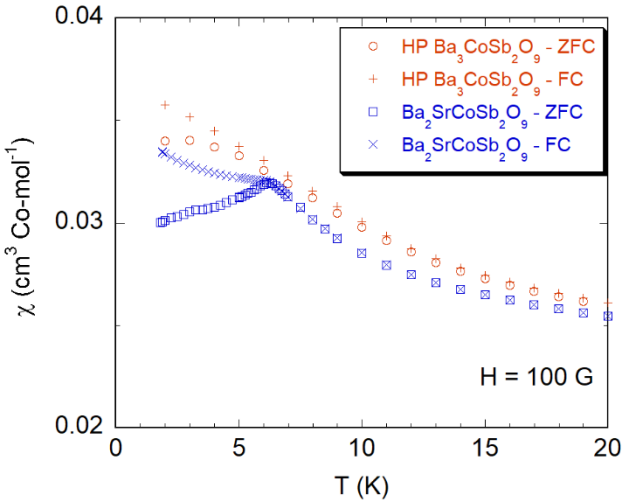

Figure 6. Variable-temperature zero-field-cooled (ZFC) and field-cooled (FC) dc magnetic susceptibility $\chi(T)$ data for HP $Ba_3CoSb_2O_9$ and $Ba_2SrCoSb_2O_9$ collected under an applied magnetic field of 100 G.

3.3 μSR and ^{121}Sb NMR for $Ba_2SrCoSb_2O_9$

We performed both μSR and NMR measurements on the same sample of $Ba_2SrCoSb_2O_9$. They gave a consistent picture of a bulk freezing much alike a spin-glass phase as detailed below.

The weak transverse field (wTF) experiments under an applied field of 50 G presented for a few typical temperatures in Fig. 7, enable one to track the paramagnetic fraction of the sample.

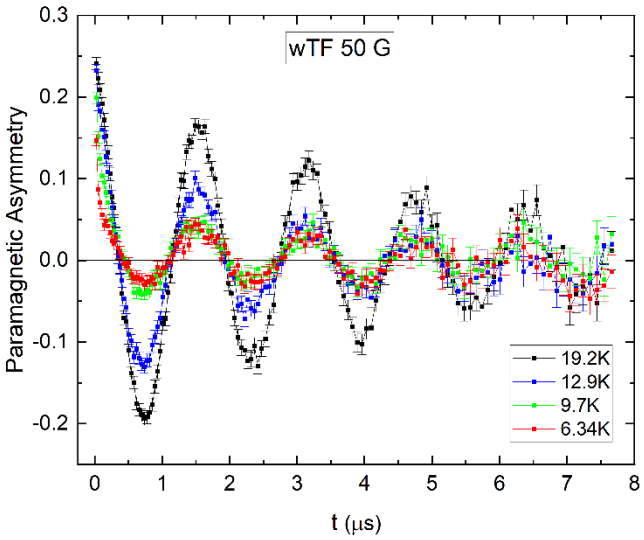

Figure 7. Evolution of the asymmetry with time under a 50 G transverse applied field for $Ba_2SrCoSb_2O_9$. The oscillations are typical of muons precessing in the external field, i.e. being in a paramagnetic environment.

The decrease of the oscillating part measured at times larger than 0.2 μs for T = 6.34 and 9.7 K is typical of a loss of response to the external field which relates to larger internal fields that develop when magnetic moments freeze in the sample. For higher temperatures, the damping of the long-time oscillations is due to relaxation effects associated with a slowing down of the spin dynamics when approaching the magnetic transition. The evolution of the relaxation is best followed by using a longitudinal field (LF) geometry under a 50 G field aimed at decoupling the nuclear contribution. The results of our analysis for both sets of experiments, TF and LF are summarized in Fig. 8.

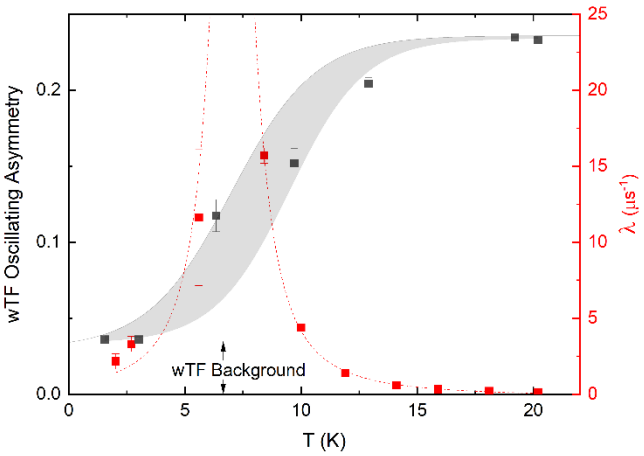

Figure 8. Left scale, black dots: temperature variation of the wTF oscillating asymmetry reflecting the paramagnetic fraction. The grey area corresponds to the uncertainty in

determining the value of that asymmetry around the transition. The maximum 0.235(1) high-temperature asymmetry value serves as a reference for a 100% paramagnetic fraction. Right scale, red dots: temperature variation of the relaxation rate λ. Its divergence is typical of a drastic slowing down of the spin dynamics at a magnetic transition.

The decrease of the wTF asymmetry is very progressive, starting below 12 K, in stark contrast with what would be expected for a very sharp phase transition. Below ~3 K and down to the 1.55 K base temperature of our experiment, the oscillating asymmetry levels off at a 0.036 (1) value, a part of which could be due to the instrument background, typically 0.01 in the veto mode. From this, one can safely conclude that at least 90% of the sample undergoes a magnetic freezing which can be attributed to the $Ba_2SrCoSb_2O_9$ phase. A divergence of the relaxation rate λ is also observed around 7 K as expected for a phase transition. Although one can expect that in the presence of a well-ordered structure, spontaneous oscillations of the asymmetry should be observed at short times under zero external field, it was not the case here (not shown). This indicates a disordered frozen ground state, much alike a spin glass.

Such conclusions are perfectly in line with the NMR results displayed in Fig. 9.

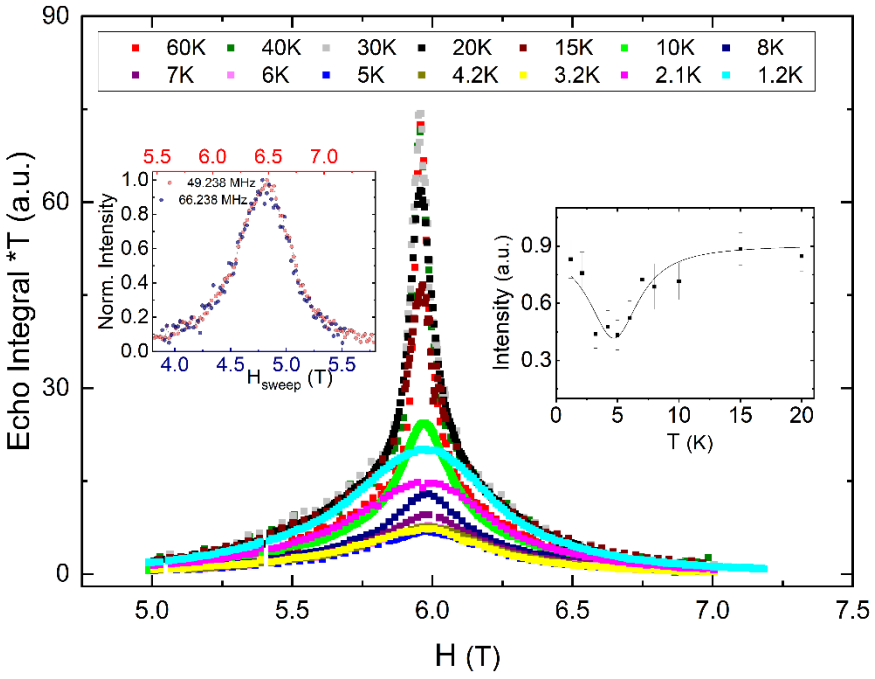

Figure 9. Main panel: Temperature evolution of the NMR spectra. The loss of integrated intensity (see text) around the transition is depicted in the right panel. The left panel shows the

superposition between two field-sweeps taken at different frequencies, at T=1.2 K. The field extension of those plots is the same for the two spectra.

From the main panel, one can see that the spectra broaden progressively starting below 12 K while their integrated intensity corrected from relaxation effects, which is a measure of the total number of nuclei which are detected, has a dip around the transition. The full width at half maximum (not shown) increases most significantly below 10 K, to reach a constant value below 4 K as expected when a freezing occurs and its associated order parameter develops. The static character is best established by the invariance of the absolute distribution of fields for the field sweep spectra taken for a frequency 66.2 and 49.2 MHz at 1.2 K, which is typical of an internal field associated with the freezing as measured on the Sb nucleus. Finally, the partial loss of intensity around the transition is a very common signature of a slowing-down of the dynamics leading to a wipe-out of the NMR signal. The fact that it occurs on an extended temperature range can be associated with the broad peak observed for the μSR relaxation rate and clearly reminds what occurs in spin glasses.

4. Discussion

We first discuss the effects of physical pressure and of chemical substitution on the crystal structure of $Ba_3CoSb_2O_9$. The external pressure, which is applied during HP synthesis, and the substitution of Sr^{2+} for bigger Ba^{2+} both contract the crystal lattice and cause the tolerance factor, *t*, to decrease. Volumes per formula unit for HP $Ba_3CoSb_2O_9$ and $Ba_2SrCoSb_2O_9$ have decreased by 15% and 17 % with respect to that of AP 6HA $Ba_3CoSb_2O_9$, respectively. The tolerance factor of ABO_3 perovskites, which is defined as $t = \frac{(r_A+r_O)}{\sqrt{2}(r_B+r_O)}$, is based on the radius of oxide ion, r_O, and on the average radii, r_A and r_B, of the ions located at the 12-coordinated A and octahedral B sites, respectively[28]. For *t* equal or very close to 1, 3C cubic structures occur. Distortions to lower symmetries are expected when $t < 1$. Hexagonal 6H structures are observed when $t > 1$. For mixed B cations $Ba_3M^{2+}Sb^{5+}O_9$ oxides where M = transition metal, the following tolerance factor ranges apply: $t > 1.03$ 6H, $0.97 < t < 1.03$ cubic[11,29]. In AP 6HA $Ba_3CoSb_2O_9$, the tolerance factor calculated using Shannon's ionic radii[23], $t = 1.04$, is indeed higher than 1.03 and close to those calculated for AP 6HA compounds $Ba_3NiSb_2O_9$ ($t = 1.05$) and $Ba_3ZnSb_2O_9$ ($t = 1.04$). External pressure tends to

decrease the tolerance factor because the Ba-O bonds are more compressible than the B-O and B'-O bonds, so that pressure-induced transformations of 6H to cubic double perovskite structures are observed in $Ba_3MSb_2O_9$ where M = Ni, Co, Zn[4,13,15]. Based on the tolerance factor, cubic phases should also be stabilized in Ba/Sr substituted compounds. For HP $Ba_3CoSb_2O_9$ and $Ba_2SrCoSb_2O_9$ the observed tolerance factors calculated from the bond lengths (Table 3), t_{obs} = 1.00 for both compounds, indeed fall within the range between 0.97 and 1.03 for which a cubic structure is generally observed[11,29]. The 6H plus cubic two-phase region observed in $Ba_{3-x}Sr_xCoSb_2O_9$ for $0.1 < x < 1$ is similar to that previously observed in $Ba_{3-x}Sr_xZnSb_2O_9$[15].

Differences between the crystal structures of HP $Ba_3CoSb_2O_9$ and $Ba_2SrCoSb_2O_9$ are associated with the Co/Sb distributions over the octahedral sites of the perovskite structure. Despite the small ionic radius difference of the Co^{2+} and the pnictogen Sb^{5+} ions, the significant charge difference is likely to favor a rock salt type arrangement of the Co and Sb cations in the structure[30–32]. Instead of being randomly distributed over all octahedral sites, Co^{2+} ions occupy mainly (in HP $Ba_3CoSb_2O_9$) or only (in $Ba_2SrCoSb_2O_9$) one of the two FCC sublattices which are formed by the B or the B' sites in the $A_2BB'O_6$ double perovskite structural model (Fig. 1). This structural difference indicates that the HP-HT treatment with relaxed external pressure is not equivalent to the chemical substitution at the Ba site. Furthermore, HP phases can be metastable at room temperature and ambient pressure[10] while it is expected that AP $Ba_2SrCoSb_2O_9$ is thermodynamically stable.

The observed magnetic properties are correlated with structural features. The double perovskite $A_2BB'O_6$ crystal structure comprises two interpenetrating B and B' FCC sublattices (Fig. 1). In $Ba_2SrCoSb_2O_9$, one of these two FCC lattice (B sites) is fully occupied by nonmagnetic Sb^{5+} ions while the other (B' sites) is occupied by a random distribution of Co^{2+} and Sb^{5+} ions with 67% site occupancy for Co atoms. This occupancy rate is higher than the site percolation threshold of the FCC sublattice (≈ 20%). Since the negative Weiss temperature suggest dominant AF interactions, $Ba_2SrCoSb_2O_9$ contains a diluted frustrated FCC sublattice of spin-3/2 Co^{2+} ions. An AF FCC lattice is based on edge-shared tetrahedra of nearest-neighbor magnetic interactions, giving rise to geometric frustration. The value of the frustration index for $Ba_2SrCoSb_2O_9$ $|\theta|/T_f \approx 19$ is rather high compared to those observed in other cation ordered double perovskites[25]. The ratio of the Weiss temperature to the magnetic ordering temperature serves as a metric in the field of frustrated materials, but it must be kept in mind that it cannot distinguish between the roles of low dimensionality (not essential in the present

case of a 3D FCC lattice) or of disorder and that of frustration. For nondiluted FCC Ising or Heisenberg antiferromagnets a transition to a long range antiferromagnetic order is expected at low temperature[25,33–35]. Considering the random dilution of the FCC sublattice and the substitution of Sr for Ba, it is not surprising to observe a disordered magnetic state at low temperature in $Ba_2SrCoSb_2O_9$. The situation regarding HP $Ba_3CoSb_2O_9$ is also complex; the Co^{2+} distribution over both the B' and B octahedral sites leads to additional complexity in magnetic interactions with B'-B', B-B, and B-B' couplings, the two latter interactions being less probable than the former. The additional B-B' interaction is expected to be dominated by an AF 180° Co-O-Co superexchange. The presence of 17% of Co^{2+} in the B sublattice also leads to the disruption of some of the 90° and 180° Co-O-Sb-O-Co superexchanges of the B' sublattice. These complex magnetic interactions are likely to explain why there is no apparent magnetic transition down to low temperature. The origin of the observed ZFC-FC magnetic irreversibility in HP $Ba_3CoSb_2O_9$ still remains unclear. Also, the possible spin-glass (or cluster glass) nature of the magnetic transition at 6 K in $Ba_2SrCoSb_2O_9$ is not firmly established from our data. Analysis of the field and frequency dependence of the magnetic susceptibilities at low temperatures will certainly help better understand the magnetic properties of these two new cubic Co-based perovskite materials.

5. Concluding remarks

In this work, a 6HA $\rightarrow$ 6HA plus cubic two-phase region $\rightarrow$ cubic perovskite sequence of structural phases was observed with increasing physical pressure applied to $Ba_3CoSb_2O_9$ or with increasing Sr content in AP $Ba_{3-x}Sr_xCoSb_2O_9$. As expected from the tolerance factor (*t*), HP $Ba_3CoSb_2O_9$ and $Ba_2SrCoSb_2O_9$ crystallize in cubic perovskite structures. Their average structures can be described in a rock salt like ordered double perovskite model with chemical chemical formulae $Ba_2Co_{2/3}Sb_{4/3}O_6$ and $Ba_{4/3}Sr_{2/3}Co_{2/3}Sb_{4/3}O_6$ for the HP and Sr-substituted compounds, respectively. Both compounds show paramagnetic behaviors down to low temperature due to geometric frustration, random distributions of Co^{2+} and nonmagnetic Sb^{5+} over octahedral sites, and disorder on the Ba site in the case of $Ba_2SrCoSb_2O_9$. Our μSR and NMR data unambiguously indicate a transition to a disordered magnetic state in $Ba_2SrCoSb_2O_9$. Further studies will be needed to better understand the magnetic properties of HP $Ba_3CoSb_2O_9$ and $Ba_2SrCoSb_2O_9$.

Declaration of competing interest

The authors declare that they have no known competing financial interests or personal relationships that could have appeared to influence the work reported in this paper.

Acknowledgments

We would like to thank Stéphane Grolleau for assistance in physicochemical characterizations. This work was supported by the French Agence Nationale de la Recherche under Grants Nos. ANR-12-BS04-0021 'SPINLIQ' and ANR-18-CE30-0022-04 'LINK'.

References

[1] C. Broholm, R.J. Cava, S.A. Kivelson, D.G. Nocera, M.R. Norman, T. Senthil, Quantum spin liquids, Science. 367 (2020) eaay0668. https://doi.org/10.1126/science.aay0668.

[2] J.R. Chamorro, T.M. McQueen, T.T. Tran, Chemistry of Quantum Spin Liquids, Chem. Rev. 121 (2021) 2898–2934. https://doi.org/10.1021/acs.chemrev.0c00641.

[3] Y. Li, P. Gegenwart, A.A. Tsirlin, Spin liquids in geometrically perfect triangular antiferromagnets, J. Phys. Condens. Matter. 32 (2020) 224004. https://doi.org/10.1088/1361-648X/ab724e.

[4] J.G. Cheng, G. Li, L. Balicas, J.S. Zhou, J.B. Goodenough, C. Xu, H.D. Zhou, High-Pressure Sequence of $Ba_3NiSb_2O_9$ Structural Phases: New S=1 Quantum Spin Liquids Based on Ni^{2+}, Phys. Rev. Lett. 107 (2011) 197204. https://doi.org/10.1103/PhysRevLett.107.197204.

[5] Y. Shirata, H. Tanaka, A. Matsuo, K. Kindo, Experimental Realization of a Spin-$1/2$ Triangular-Lattice Heisenberg Antiferromagnet, Phys. Rev. Lett. 108 (2012) 057205. https://doi.org/10.1103/PhysRevLett.108.057205.

[6] H.D. Zhou, C. Xu, A.M. Hallas, H.J. Silverstein, C.R. Wiebe, I. Umegaki, J.Q. Yan, T.P. Murphy, J.-H. Park, Y. Qiu, J.R.D. Copley, J.S. Gardner, Y. Takano, Successive Phase Transitions and Extended Spin-Excitation Continuum in the S=1/2 Triangular-Lattice Antiferromagnet $Ba_3CoSb_2O_9$, Phys. Rev. Lett. 109 (2012) 267206. https://doi.org/10.1103/PhysRevLett.109.267206.

[7] H.D. Zhou, E.S. Choi, G. Li, L. Balicas, C.R. Wiebe, Y. Qiu, J.R.D. Copley, J.S. Gardner, Spin Liquid State in the S=1/2 Triangular Lattice $Ba_3CuSb_2O_9$, Phys. Rev. Lett. 106 (2011) 147204. https://doi.org/10.1103/PhysRevLett.106.147204.

[8] S. Nakatsuji, K. Kuga, K. Kimura, R. Satake, N. Katayama, E. Nishibori, H. Sawa, R. Ishii, M. Hagiwara, F. Bridges, T.U. Ito, W. Higemoto, Y. Karaki, M. Halim, A.A. Nugroho, J.A. Rodriguez-Rivera, M.A. Green, C. Broholm, Spin-Orbital Short-Range Order on a Honeycomb-Based Lattice, Science. 336 (2012) 559–563. https://doi.org/10.1126/science.1212154.

[9] J.A. Quilliam, F. Bert, E. Kermarrec, C. Payen, C. Guillot-Deudon, P. Bonville, C. Baines, H. Luetkens, P. Mendels, Singlet Ground State of the Quantum Antiferromagnet $Ba_3CuSb_2O_9$, Phys. Rev. Lett. 109 (2012). https://doi.org/10.1103/PhysRevLett.109.117203.

[10] J.B. Goodenough, J.A. kafalas, Exploring the $A^+B^{5+}O_3$ compounds, J. Solid State Chem. 6 (1973) 493–501. https://doi.org/10.1016/S0022-4596(73)80005-2.

[11] A.J. Jacobson, A.J. Calvert, A powder neutron diffraction study of cation ordering in 6H $Ba_3Sb_2NiO_9$, J. Inorg. Nucl. Chem. 40 (1978) 447–449. https://doi.org/10.1016/0022-1902(78)80421-7.
[12] H. Man, M. Halim, H. Sawa, M. Hagiwara, Y. Wakabayashi, S. Nakatsuji, Spin-orbital entangled liquid state in the copper oxide $Ba_3CuSb_2O_9$, J. Phys. Condens. Matter. 30 (2018) 443002. https://doi.org/10.1088/1361-648X/aae106.
[13] P.D. Battle, C.W. Jones, P. Lightfoot, R. Strange, High-pressure phase transitions in the 6H perovskites $Ba_3MSb_2O_9$ (M =Mg, Ni, Zn), J. Solid State Chem. 85 (1990) 144–150. https://doi.org/10.1016/S0022-4596(05)80069-6.
[14] J.A. Quilliam, F. Bert, A. Manseau, C. Darie, C. Guillot-Deudon, C. Payen, C. Baines, A. Amato, P. Mendels, Gapless quantum spin liquid ground state in the spin-1 antiferromagnet 6HB $Ba_3NiSb_2O_9$, Phys. Rev. B. 93 (2016) 214432. https://doi.org/10.1103/PhysRevB.93.214432.
[15] J. Li, P. Jiang, W. Gao, R. Cong, T. Yang, Chemical Substitution-Induced and Competitive Formation of 6H and 3C Perovskite Structures in $Ba_{3-x}Sr_xZnSb_2O_9$: The Coexistence of Two Perovskites in $0.3 \leq x \leq 1.0$, Inorg. Chem. 56 (2017) 14335–14344. https://doi.org/10.1021/acs.inorgchem.7b02429.
[16] Q. Huang, R. Rawl, W.W. Xie, E.S. Chou, V.S. Zapf, X.X. Ding, C. Mauws, C.R. Wiebe, E.X. Feng, H.B. Cao, W. Tian, J. Ma, Y. Qiu, N. Butch, H.D. Zhou, Non-magnetic ion site disorder effects on the quantum magnetism of a spin-1/2 equilateral triangular lattice antiferromagnet, J. Phys. Condens. Matter. 34 (2022) 205401. https://doi.org/10.1088/1361-648X/ac5703.
[17] S.Y. Istomin, V.A. Koutcenko, E.V. Antipov, F. Lindberg, G. Svensson, Synthesis and characterization of novel 6-H perovskites $Ba_2Co_{2-x}Sb_xO_{6-y}$, $0.6 \leq x \leq 0.8$ and $x = 1.33$ ($Ba_3CoSb_2O_9$), Mater. Res. Bull. 39 (2004) 1013–1022. https://doi.org/10.1016/j.materresbull.2004.03.009.
[18] Y. Doi, Y. Hinatsu, K. Ohoyama, Structural and magnetic properties of pseudo-two-dimensional triangular antiferromagnets $Ba_3MSb_2O_9$ (M = Mn, Co, and Ni), J. Phys. Condens. Matter. 16 (2004) 8923–8935. https://doi.org/10.1088/0953-8984/16/49/009.
[19] P. Suortti, Effects of porosity and surface roughness on the X-ray intensity reflected from a powder specimen, J. Appl. Crystallogr. 5 (1972) 325–331. https://doi.org/10.1107/S0021889872009707.
[20] V. Petricek, M. Dusek, L. Palatinus, Crystallographic Computing System JANA2006: General features, Z. Für Krist. 229 (2014) 345–352. https://doi.org/10.1515/zkri-2014-1737.
[21] J. Rodríguez-Carvajal, Recent advances in magnetic structure determination by neutron powder diffraction, Phys. B Condens. Matter. 192 (1993) 55–69. https://doi.org/10.1016/0921-4526(93)90108-I.
[22] I.D. Brown, D. Altermatt, Bond-valence parameters obtained from a systematic analysis of the Inorganic Crystal Structure Database, Acta Crystallogr. B. 41 (1985) 244–247. https://doi.org/10.1107/S0108768185002063.
[23] R.D. Shannon, Revised effective ionic radii and systematic studies of interatomic distances in halides and chalcogenides, Acta Crystallogr. A. 32 (1976) 751–767. https://doi.org/10.1107/S0567739476001551.
[24] P.D. Battle, J.G. Gore, R.C. Hollyman, A.V. Powell, The magnetic properties of $BaLaCoIrO_6$ and $Ba_3CoIr_xRu_{2-x}O_9$, J. Alloys Compd. 218 (1995) 110–116. https://doi.org/10.1016/0925-8388(94)01368-3.
[25] J.-W.G. Bos, J.P. Attfield, Magnetic frustration in $(LaA)CoNbO_6$ (A=Ca, Sr, and Ba) double perovskites, Phys. Rev. B. 70 (2004) 174434. https://doi.org/10.1103/PhysRevB.70.174434.

[26] M.E. Lines, Magnetic Properties of $CoCl_2$ and $NiCl_2$, Phys. Rev. 131 (1963) 546–555. https://doi.org/10.1103/PhysRev.131.546.
[27] J.A. Mydosh, Spin Glasses: An Experimental Introduction, CRC Press, London, 2014. https://doi.org/10.1201/9781482295191.
[28] V.M. Goldschmidt, Die Gesetze der Krystallochemie, Naturwissenschaften. 14 (1926) 477–485. https://doi.org/10.1007/BF01507527.
[29] J.E. Joy, E. Atamanik, R. Mani, A. Nag, R.M. Tiwari, V. Thangadurai, J. Gopalakrishnan, $Ba_3M^{III}TiM^{V}O_9$ (M^{III} = Fe, Ga, Y, Lu; MV = Nb, Ta, Sb) perovskite oxides: Synthesis, structure and dielectric properties, Solid State Sci. 12 (2010) 1970–1976. https://doi.org/10.1016/j.solidstatesciences.2010.08.009.
[30] M.T. Anderson, K.B. Greenwood, G.A. Taylor, K.R. Poeppelmeier, B-cation arrangements in double perovskites, Prog. Solid State Chem. 22 (1993) 197–233. https://doi.org/10.1016/0079-6786(93)90004-B.
[31] G. King, P.M. Woodward, Cation ordering in perovskites, J. Mater. Chem. 20 (2010) 5785–5796. https://doi.org/10.1039/B926757C.
[32] S. Vasala, M. Karppinen, $A_2B'B''O_6$ perovskites: A review, Prog. Solid State Chem. 43 (2015) 1–36. https://doi.org/10.1016/j.progsolidstchem.2014.08.001.
[33] M.S. Seehra, T.M. Giebultowicz, Magnetic structures of fcc systems with nearest-neighbor and next-nearest-neighbor exchange interactions, Phys. Rev. B. 38 (1988) 11898–11900. https://doi.org/10.1103/PhysRevB.38.11898.
[34] A.D. Beath, D.H. Ryan, Thermodynamic properties of the fcc Ising antiferromagnet obtained from precision density of states calculations, Phys. Rev. B. 73 (2006) 174416. https://doi.org/10.1103/PhysRevB.73.174416.
[35] N.-N. Sun, H.-Y. Wang, The J1-J2 model on the face-centered-cubic lattices, J. Magn. Magn. Mater. 454 (2018) 176–184. https://doi.org/10.1016/j.jmmm.2018.01.076.